

See discussions, stats, and author profiles for this publication at: <https://www.researchgate.net/publication/236112929>

Gas-Phase Self-Assembly of Highly Ordered Titania@Graphene Nanoflakes for Enhancement in Photocatalytic Activity

ARTICLE in ACS APPLIED MATERIALS & INTERFACES · MAY 2013

Impact Factor: 6.72 · DOI: 10.1021/am400765z · Source: PubMed

CITATIONS

15

READS

96

2 AUTHORS, INCLUDING:



Jeong Hoon Byeon

Yeungnam University

89 PUBLICATIONS 997 CITATIONS

SEE PROFILE

Gas-Phase Self-Assembly of Highly Ordered Titania@Graphene Nanoflakes for Enhancement in Photocatalytic Activity

Jeong Hoon Byeon[†] and Young-Woo Kim^{*,‡}

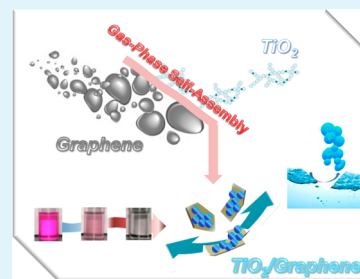
[†]Department of Chemistry, Purdue University, West Lafayette, Indiana 47907, United States

[‡]Department of Automotive Engineering, Hoseo University, Asan 336-795, Republic of Korea

S Supporting Information

ABSTRACT: The gas-phase self-assembly of reduced graphene oxide (rGO) nanoflakes with highly ordered ultrafine titania (TiO₂) particles was performed and the resultant hybrid material displayed an enhanced photocatalytic performance, both in producing hydrogen and in degrading dyes. Freshly synthesized TiO₂ nanoparticles (~35 nm in equivalent mobility diameter) were quantitatively incorporated with nanoscale rGO (~36 nm in equivalent mobility diameter) in the form of TiO₂/rGO hybrid nanoflakes (~31 nm in equivalent mobility diameter). The TiO₂/rGO hybrid flakes were finally employed to evaluate its photocatalytic activity, and it was found that the ability to achieve hydrogen production and dye degradation was greater than that of a hybridized material from commercial p25-TiO₂ and large rGO. This gas-phase self-assembly also enhanced the photocatalytic activity by applying different spark configurations to prepare ZnO, Au, or Ag particles incorporated with rGO nanoflakes.

KEYWORDS: aerosol fabrication, graphene, hybrid nanoparticles, photocatalytic performance, hydrogen production, dye degradation



INTRODUCTION

Graphene (more accurately called reduced GO (rGO)) has attracted much interest for its unique physical and chemical properties and wide-ranging technological applications.^{1–3} Interest in nanocomposites and hybrid nanomaterials has been ever-growing, which is ascribed to their peculiarities in combining the desirable properties of building blocks for a given application.⁴ Besides the applications of rGO, there is a great desire to fabricate composites or hybrid materials that integrate rGO with nanoparticles, polymers, and even nanotubes and fullerenes.⁵

It is of great importance to bind metallic nanoparticles onto rGO because the combination and interaction between the nanoparticles and rGO will lead to multifunctional or even completely new properties in such a nanocomposite.⁶ Metallic nanoparticles incorporating rGO hybrid materials were recently introduced as active materials for environmental,⁷ energy,⁸ and biological applications.⁹ In particular, the hybridization of titania (TiO₂) with rGO has been proposed as a suitable method for increasing the photocatalytic activity.^{10,11} However, the nanoparticle hybridization with rGO requires additional batch chemical steps and controls for the preparation of the nanoparticles,^{12–14} and thus it is still a challenge to prepare the nanoparticle/rGO hybrid materials under a green and continuous synthesis manner. Nanometer-sized (<several tens of nanometers) graphene sheets have recently received much attention, especially in cellular imaging and drug delivery,¹⁵ because of their size-matching interface with biological systems and the high stability of graphene in aqueous environments. To the best of our knowledge, this is the first attempt to hybridize

rGO nanoflakes and ultrafine TiO₂ particles in a continuous gas-phase manner for efficient photocatalytic applications.

The present work introduces a continuous gas-phase self-assembly of TiO₂/rGO hybrid nanoflakes for an enhancement of photocatalytic hydrogen production and dye degradation. A spark discharge produced TiO₂ nanoparticles, and the particle-laden flow passed over the collision atomizer orifice where they mixed with the atomized rGO solution to form hybrid droplets. The droplets then passed through a heated tube reactor to drive solvent from the droplets, resulting in TiO₂/rGO hybrid nanoflakes. The combination of rGO nanoflakes and ultrafine TiO₂ particles in a hybrid nanostructure enhanced the interfacial contact between them. The hybrid nanoflakes were separated using mechanical filtration, and finally they were employed as photocatalysts to produce hydrogen and to degrade dye. The photocatalytic activities of the nanoflakes and hybrid materials from commercial TiO₂ and rGO are systematically compared and discussed.

METHODS

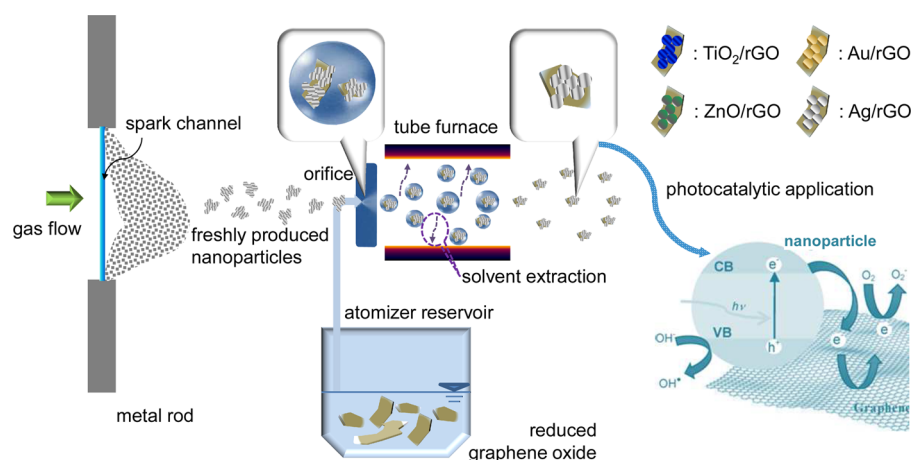
As shown in Scheme 1, a spark discharge was used to generate aerosol TiO₂ nanoparticles, and the particle laden flow was employed as the operating gas for atomizing the rGO solution. The GO nanoflakes were produced via serial processes of graphite nanoparticles from another spark discharge with a modified Hummer's reaction and a photoreduction in ethanol (refer to the Supporting Information). The specifications of the spark discharge configuration were as follows:

Received: February 28, 2013

Accepted: April 4, 2013

Published: April 4, 2013

Scheme 1. Continuous Gas-Phase Self-Assembly of Graphene Nanoflakes with TiO₂ Nanoparticles for Photocatalytic Applications; Other Nanoparticles (ZnO, Au, and Ag) were Also Incorporated with Graphene Nanoflakes via the Same Method



electrode diameter (C-072561, Nilaco, Japan) and length, 3 mm and 100 mm, respectively; resistance, 0.5 M Ω ; capacitance, 1.0 nF; loading current, 2.0 mA; applied voltage, 3.0 kV; and frequency, 667 Hz. The immersed GO particles as a dispersion were then treated with UV (306 nm) irradiation. During this treatment, the hydrated electron acts as a reducing agent to reduce GO to rGO. This is because water exhibits a high absorption cross-section for UV irradiation and homolyzes upon excitation into hydrogen atoms, hydroperoxyl radicals, and hydrated electrons.³ Because of the continuous manner of the present method, the dispersity of rGO in the solution was simply maintained by mechanical stirring in the absence of stabilizer, such as polyvinylpyrrolidone. The TiO₂ particles (from another spark discharge between titanium rods (TI-452564, Nilaco, Japan) under air flow) passed over the atomizer orifice, where they mixed with atomized rGO droplets to form hybrid droplets. The droplets then passed through a heated tubular reactor (GTF 12/25/364, Lenton Furnaces, UK) to drive solvent from the droplets. The resulting TiO₂/rGO hybrid flakes were separated from the flow via mechanical filtration. They were set aside in a clean booth to keep them in a powder form.

To measure photoelectrochemical responses, we dispersed 5 mg of TiO₂/rGO hybrid nanoflakes in 5 mL of ethanol. After 10 min of sonication, the nanoflakes were coated onto a 2 cm² indium–tin oxide (ITO) glass electrode and dried at 25 °C. The prepared electrodes, saturation calomel electrode, and Pt electrode were chosen as the working, reference, and counter electrodes, respectively. The electrolyte was 0.5 M L⁻¹ Na₂SO₄ aqueous solution. The working electrode was irradiated horizontally by a high pressure mercury lamp (160 W) and a cutoff filter ($\lambda > 400$ nm). Photocatalytic hydrogen production was carried out in aqueous suspension under visible light ($\lambda > 400$ nm). The filtered light was collected in the headspace of the closed reactor and analyzed by a gas chromatograph (3000, Agilent, US) with a thermal conductivity detector and Ar used as carrier gas. The photocatalytic degradation of rhodamine B (RhB) in the presence of TiO₂/rGO was investigated by irradiating aqueous solutions of the dye molecule (10 mL, 1×10^{-4} M) containing suspended TiO₂/rGO nanoparticles (0.4 mg mL⁻¹) with visible light (via a 250 W high pressure mercury lamp equipped with a 400 nm cutoff filter) while stirring with a magnetic bar. Prior to the irradiation, the suspension was magnetically stirred in the dark for 30 min in order to reach an adsorption–desorption equilibrium. For comparison purposes, photocatalytic degradation of RhB was also carried out in the presence of commercial TiO₂ (p25, Degussa, Germany) incorporated with large rGO (L-rGO, G250, Sinocarbon, China) sheets. The concentration was monitored by UV–vis absorption spectroscopy (330, Perkin-Elmer, US) through changes in the absorption peak at 554 nm.

RESULTS AND DISCUSSION

To prepare fresh TiO₂ nanoparticles first, a spark discharge under air environment was employed. The gas temperature

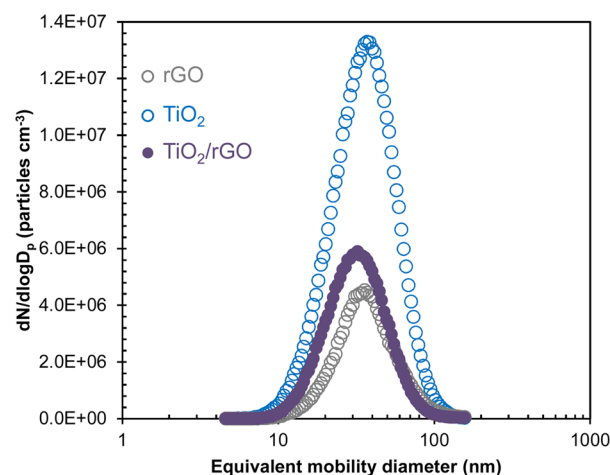


Figure 1. Size distributions of collision-atomized rGO, spark-produced TiO₂, and their hybridized nanostructures (TiO₂/rGO) in the gas-phase. Standard deviations are noted in Table 1.

Table 1. Summary of the Size Distributions of Collision-Atomized rGO, Spark-Produced TiO₂, and their Hybridized Nanostructures (TiO₂/rGO) in the Gas-Phase

case	GMD (nm)	GSD	TNC ($\times 10^6$ particles cm ⁻³)
rGO	36.1	1.57	1.99
TiO ₂	34.7	1.59	6.66
TiO ₂ /rGO	31.4	1.54	2.81

inside the spark channel was increased beyond a critical value, which was sufficient to sublime parts of the Ti electrodes.¹⁶ The duration of each spark was very short (~ 1 ms) and the vapors cooled rapidly downstream of the spark. This formed a supersaturation resulting in particle formation through nucleation–condensation. The total number concentration (TNC), geometric mean diameter (GMD), and geometric standard deviation (GSD) of the TiO₂ particles, which were measured using a scanning mobility particle sizer (SMPS, 3936, TSI, US), were 6.66×10^6 particles cm⁻³, 34.7 nm, and 1.59,

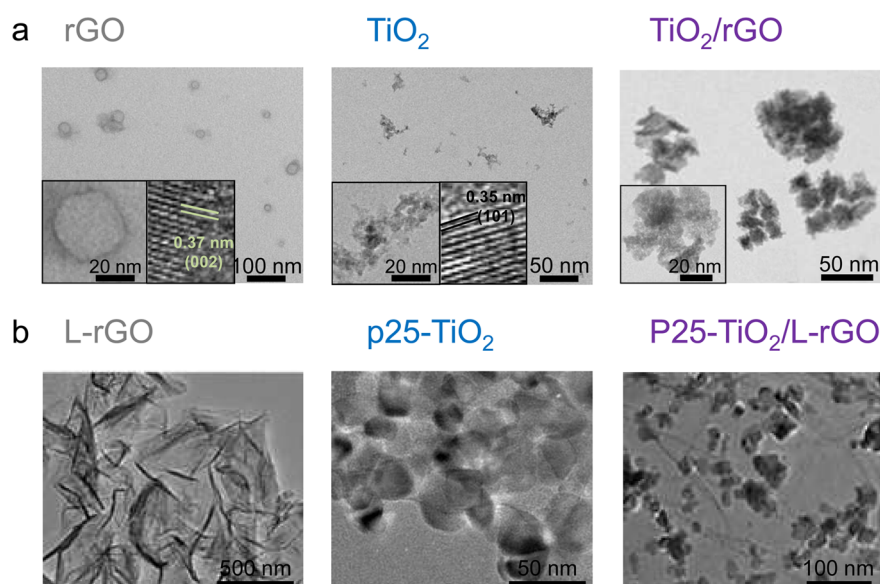


Figure 2. TEM images of (a) continuously gas-phase synthesized rGO (33 ± 7.9 nm), TiO₂ (28 ± 5.1 nm), and TiO₂/rGO (31 ± 6.8 nm) and (b) other hybrid materials ($1,188 \pm 96.6$ nm) using commercial p25-TiO₂ (29 ± 4.2 nm) and large rGO (L-rGO) ($1,253 \pm 109.3$ nm).

respectively, as shown in Figure 1. TiO₂/rGO hybrid nanoflakes were formed by incorporating TiO₂ with rGO during the collision atomization of the rGO solution. We verified the incorporation of the TiO₂ nanoparticles with the rGO nanoflakes by measuring the size distributions of the rGO and TiO₂/rGO flakes in the gas-phase. Table 1 summarizes the size distribution measurements of the rGO and TiO₂/rGO flakes. The GMD, GSD, and TNC of the TiO₂/rGO hybrid flakes were 2.81×10^6 particles cm⁻³, 31.4 nm, and 1.54, respectively. The analogous data for rGO were 1.99×10^6 cm⁻³, 36.1 nm, and 1.57, respectively. The size distribution of the TiO₂/rGO was rather similar to the rGO particles compared to that of the TiO₂ particles, and there was no bimodal distribution character, implying that the TiO₂ particles were nearly quantitatively incorporated with the rGO, to form TiO₂/rGO hybrid flakes.

Low- and high-magnification transmission electron microscope (TEM, JEM-3010, JEOL, Japan) images show the morphology of rGO, TiO₂, and TiO₂/rGO. Specimens were prepared for examination in the TEM by direct electrostatic gas-phase sampling at a sampling flow of 1.0 L min⁻¹ and an operating voltage of 5 kV using a Nano Particle Collector (NPC-10, HCT, Korea). The morphology of the rGO was as flakes, and the flake size was about 33 nm in lateral dimension with about 0.35 nm in the *d*-spacing (see inset). The TEM images (Figure 2a) also reveal that the TiO₂ particles were agglomerates (~ 28 nm in lateral dimension) of several primary particles (each ~ 3.3 nm in lateral dimension), which is consistent with the SMPS data (measured agglomerated TiO₂ particles) noted in Table 1. As shown in the inset of Figure 2a, about 0.35 nm size of the lattice fringe of TiO₂ is observed, which can be indexed as the (101) plane of the tetragonal structure. The crystalline structure of TiO₂ was further analyzed using X-ray diffraction (see Figure S2 in the Supporting Information). From energy dispersive X-ray (EDX, JED-2200, JEOL, Japan) analyses, in addition, the chemical formula of the TiO₂ particles can be defined as TiO_{1.94}. When the TiO₂ particles passed over the orifice of the collision atomizer, most TiO₂ particles were attached to the rGO flakes, resulting in TiO₂/rGO hybrid nanoflakes. The TEM image shows larger

sizes of the hybrid nanoflakes owing to gathering individual hybrid flake during the direct electrostatic gas-phase sampling. Nevertheless, the TiO₂ particles were redistributed on the rGO flakes as a highly ordered configuration due to deagglomeration (by setting the force acting on an agglomerate of size D_{pa} due to the sudden pressure change across an orifice in the collision atomizer), and the size is given by^{17–19}

$$D_{pr} = \alpha \sqrt{\frac{D_{pa} H}{6\pi \Delta P \Theta^2}} \quad (1)$$

where D_{pr} is the size of a restructured agglomerate, α is the proportionality constant, H is the Hamaker constant, ΔP is the pressure difference between the front and the rear of the orifice, and Θ is the parameter controlling the maximum cohesive strength between the constituting particles in an agglomerate. TiO₂ agglomerates pass through the orifice, and the rapid changes in pressure, density, and velocity across the orifice produce an impulse capable of shattering the agglomerates. It seems that the incorporation of TiO₂ with rGO inhibited a dislocation of TiO₂ from the rGO during the gas-phase synthesis. This is probably due to the capillary ($F_{cap} = 4\pi r_p \gamma \cos \theta$, where r_p , γ , and θ are the particle radius, surface tension, and contact angle between the TiO₂ and rGO, respectively) and electrostatic attraction ($F_{ea} = 1/(4\pi\epsilon_0)(q_1 q_2)/(d^2)$, where ϵ_0 is the permittivity constant, d is the distance between the TiO₂ and rGO, and q_1 and q_2 are surface charges of the TiO₂ and rGO, respectively) forces between the TiO₂ and rGO. Spark produced particles normally have positive charges owing to a photo- and/or electric-induced ionization of their surface during spark particle formation.²⁰ In addition, rGO has negative charges from the remaining carboxylates on its structure.²¹ The production yield of TiO₂/rGO from the gas-phase assembly is approximately 89.4%. The yield was determined by the area fraction of TiO₂/rGO-to-all particles in the TEM image. The mass content of rGO in TiO₂/rGO was $\sim 4.1\%$. Figure 2b shows TEM images of commercial graphene, TiO₂, and their hybridized structures. The morphology of L-rGO consists of thin stacked sheets and it also has a well-defined few-layer structure at the edge. p25-TiO₂/L-rGO was prepared by a

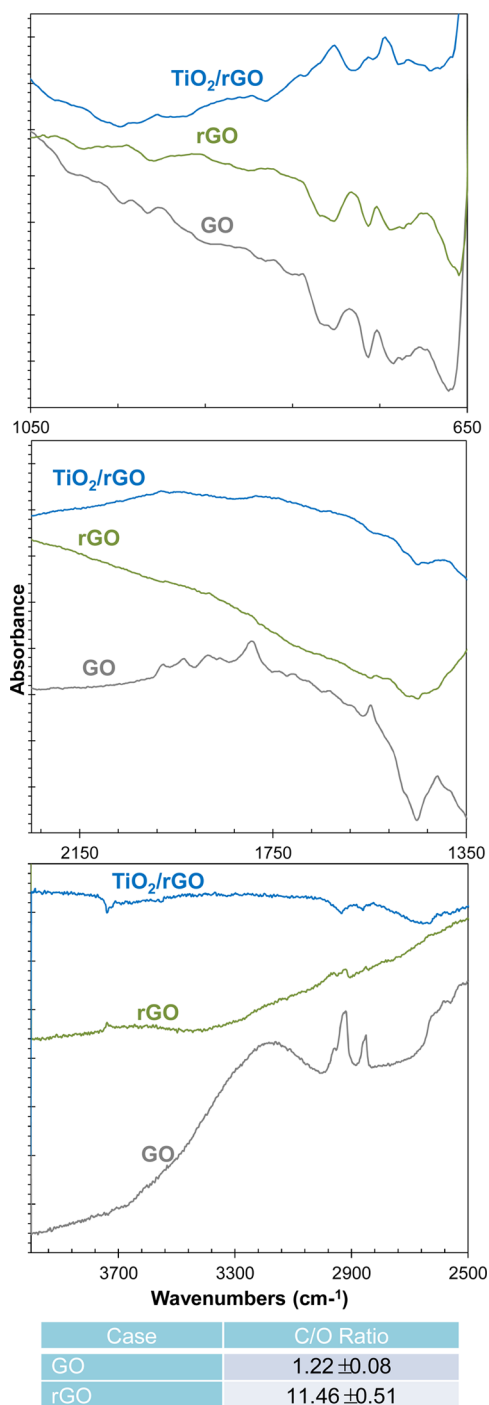


Figure 3. FTIR spectra of the GO, rGO, and TiO₂/rGO hybrid nanoflakes. C/O atomic ratio from EDX measurements is also displayed.

simple mixing of commercial p25-TiO₂ and L-rGO powders in ethanol under sonication. The hybrid material reveals a dispersion of p25-TiO₂ (~30 nm in lateral dimension) in the L-rGO matrix (~1.3 μm in lateral dimension), which has a tendency to accumulate along the wrinkles and edges of the visible graphene sheets.

Figure 3 displays Fourier transform infrared spectra (IFS 66/S, Bruker Optics, Germany) of GO, rGO, and TiO₂/rGO nanoflakes. GO exhibits broad IR peaks at around 3400 and 1730 cm⁻¹ corresponding to the O–H stretching and C=C vibrations, respectively, and also shows carboxyl C=O (1780

cm⁻¹), hydroxyl C–OH (1390 cm⁻¹), and alkoxy C–O (1050 cm⁻¹) stretching vibrations of COOH groups. rGO shows a featureless spectrum at the given absorbance scales, implying a reduction in the amount of oxygen functionalities. The spectrum of rGO was not significantly changed after the incorporation of TiO₂ particles, but new bands at around 800 cm⁻¹ correspond to Ti–O and TiO₂ stretching,^{8,22} clarifying that TiO₂ nanocrystals exist within the hybrid nanoflakes. Figure 3 also shows the degree of reduction of the GO nanoflakes. From the EDX analyses of GO and rGO, the carbon/oxygen (C/O) atomic ratio of GO was ~1.2, whereas the ratio of rGO was ~11.5, indicating that many oxygen atoms were removed by the reduction process. Other characterizations were also verified the hybrid structure of TiO₂ and rGO (see Figure S2 in the Supporting Information).

Figure 4a gives the photoelectricity results of the p25-TiO₂, p25-TiO₂/L-rGO, and TiO₂/rGO samples using a photocurrent test with a cutoff filter. The potential of the working electrode against the Pt counter electrode is set at 0.0 V. It was observed that there was a fast and uniform photocurrent responding to each turn-on and -off event in both electrodes. The photocurrents of the p25-TiO₂ and p25-TiO₂/L-rGO samples were 0.014 and 0.146 μA, respectively. This indicates that the incorporation could be effectively excited under visible light irradiation and subsequently separate photoinduced electrons and holes to enhance photocurrent. The current of p25-TiO₂ was enhanced more than 10 times by incorporation with L-rGO, and the gas-phase self-assembly further induced an enhancement of the photoelectrochemical response (0.232 μA). The time profiles of hydrogen production are compared among samples in Figure 4b. Compared with p25-TiO₂, the hybridized samples enhanced the hydrogen production performance. The hybridization assisted the photocatalysis by withdrawing electrons and subsequently retarding the charge pair recombination. Earlier studies have also explained that the enhanced photocatalytic activity of the TiO₂/rGO hybrid materials is mainly attributed to the inhibition of charge recombination.^{10,23} The present gas-phase self-assembly further enhanced the hydrogen production, which might be ascribed to the morphological difference between p25-TiO₂/L-rGO and TiO₂/rGO (from the gas-phase self-assembly). This implies that the gas-phase self-assembly between rGO nanoflakes and ultrafine TiO₂ particles did make a more appropriate structure for a better photocatalytic performance. Therefore, the photogenerated conduction band electrons in TiO₂ could be more easily transferred to rGO nanoflakes than L-rGO, because there is better contact between the TiO₂ surface and the rGO nanoflakes, whereas only a small fraction of the TiO₂ surface is in direct contact with L-rGO. Figure 4c plots the relative changes in the concentration of aqueous RhB solution as a function of the reaction time. Similar to hydrogen production, photocatalytic RhB degradation was prompted by the TiO₂/rGO, and it was also achieved in the presence of commercial samples of p25-TiO₂ and p25-TiO₂/L-rGO. The rate constant for the present catalyst was calculated to be about 6.43 × 10⁻³ min⁻¹, which is greater than those of p25-TiO₂ (3.64 × 10⁻³ min⁻¹) and p25-TiO₂/L-rGO (5.36 × 10⁻³ min⁻¹). The corresponding dye adsorption rates²⁴ of p25-TiO₂, p25-TiO₂/L-rGO and TiO₂/rGO were 10.9%, 16.1% and 19.3%, respectively. A TiO₂/rGO hybrid structure in a previous report⁷ took short time for the dye degradation compared to the present catalyst. This difference may have originated from difference in rGO content in TiO₂/rGO nanoflakes (i.e., ~4%

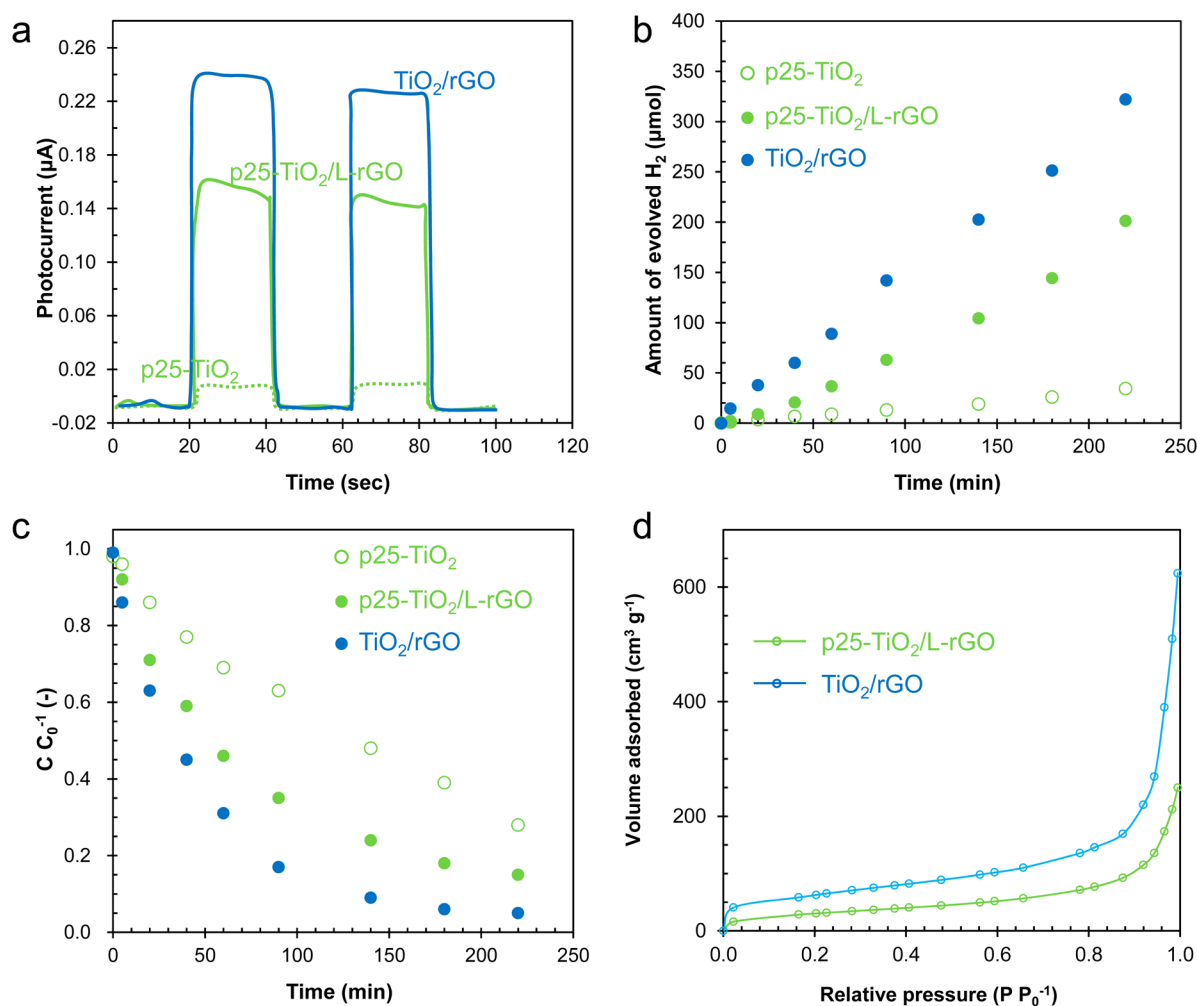


Figure 4. Photocatalytic performances of TiO₂/rGO hybrid nanoflakes in hydrogen production and dye degradation. (a) Photoelectrochemical responses of p25-TiO₂ ($0.014 \pm 0.002 \mu\text{A}$), p25-TiO₂/L-rGO ($0.146 \pm 0.021 \mu\text{A}$), and TiO₂/rGO ($0.232 \pm 0.034 \mu\text{A}$) samples. (b) Time profiles of hydrogen production with p25-TiO₂ ($0.156 \pm 0.014 \mu\text{mol min}^{-1}$), p25-TiO₂/L-rGO ($0.914 \pm 0.092 \mu\text{mol min}^{-1}$), and TiO₂/rGO ($1.464 \pm 0.129 \mu\text{mol min}^{-1}$) samples. (c) Photocatalytic degradations of RhB by p25-TiO₂ ($3.64 \times 10^{-3} \pm 0.26 \times 10^{-3} \text{ min}^{-1}$), p25-TiO₂/L-rGO ($5.36 \times 10^{-3} \pm 0.52 \times 10^{-3} \text{ min}^{-1}$), and TiO₂/rGO ($6.43 \times 10^{-3} \pm 0.48 \times 10^{-3} \text{ min}^{-1}$) samples. (d) Adsorption isotherms of p25-TiO₂/L-rGO ($156 \pm 18.9 \text{ m}^2 \text{ g}^{-1}$) and TiO₂/rGO ($289 \pm 22.0 \text{ m}^2 \text{ g}^{-1}$) samples.

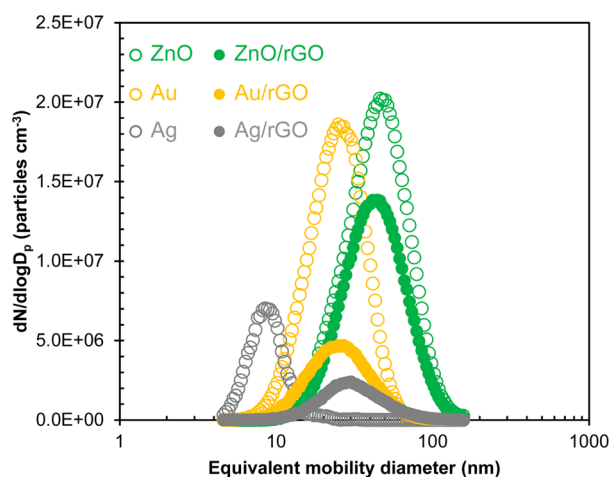


Figure 5. Size distributions of spark produced ZnO, Au, and Ag, and their hybridized nanostructures with rGO nanoflakes in the gas phase. Standard deviations are noted in Table 2.

for the present vs $\sim 2\%$ for the previous). The dye was first excited to ^1dye , followed by an electron transfer from the ^1dye to the rGO. Because of the interaction (electrostatic attraction and π - π interaction) between the dye molecules and the rGO, the dye molecules are expected to readily adsorb onto the rGO.¹⁷ The electron then moves to a TiO₂ particle and is trapped by oxygen to produce various reactive oxygen species (ROS), and the ROS finally degraded the dye. On the other hand, there were differences in performance between photocurrent and dye degradation. The difference in dye degradation was smaller than that in photocurrent, which might have originated from the different measurement conditions. In the photocurrent measurement, the magnitude of the current is related to water oxidation by the photoholes (through the formation of OH radicals), whereas in the presence of dye the holes may also be captured by the pollutant causing direct photooxidation reactions.²⁵ This might induce a different kinetic balance between the electron-hole recombination and redox reaction and therefore derives the efficiency of the degradation process. In all the previous studies of rGO and TiO₂ hybrid materials, TiO₂ particles were dispersed on the large graphene sheet (approximately micrometer-size). The

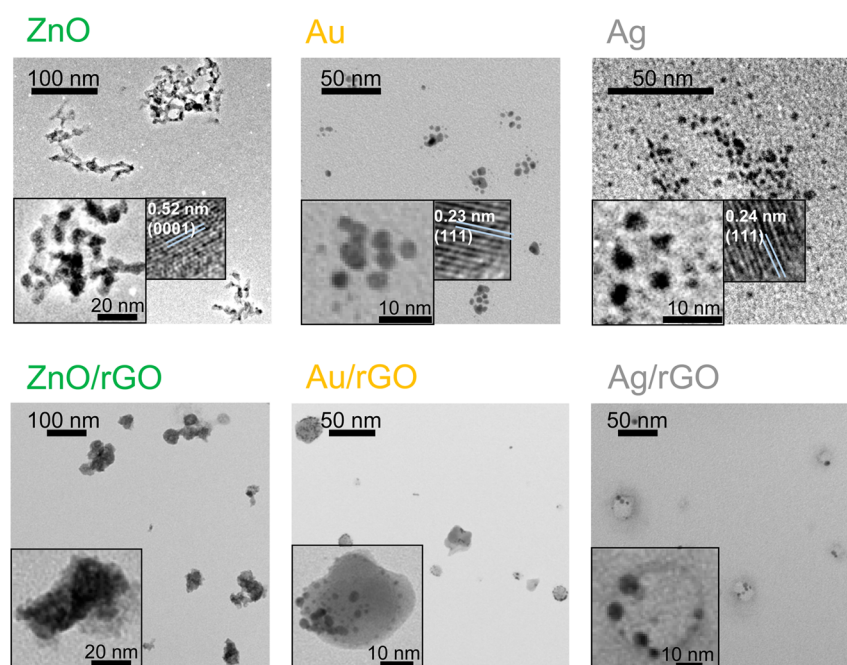


Figure 6. TEM images of continuously gas-phase synthesized other hybridized nanostructures (31 ± 3.4 nm (ZnO/rGO), 30 ± 2.9 nm (Au/rGO), and 32 ± 1.0 nm (Ag/rGO)) of ZnO (43 ± 7.2 nm), Au (21 ± 2.3 nm), or Ag (11 ± 1.4 nm) particles and rGO nanoflakes.

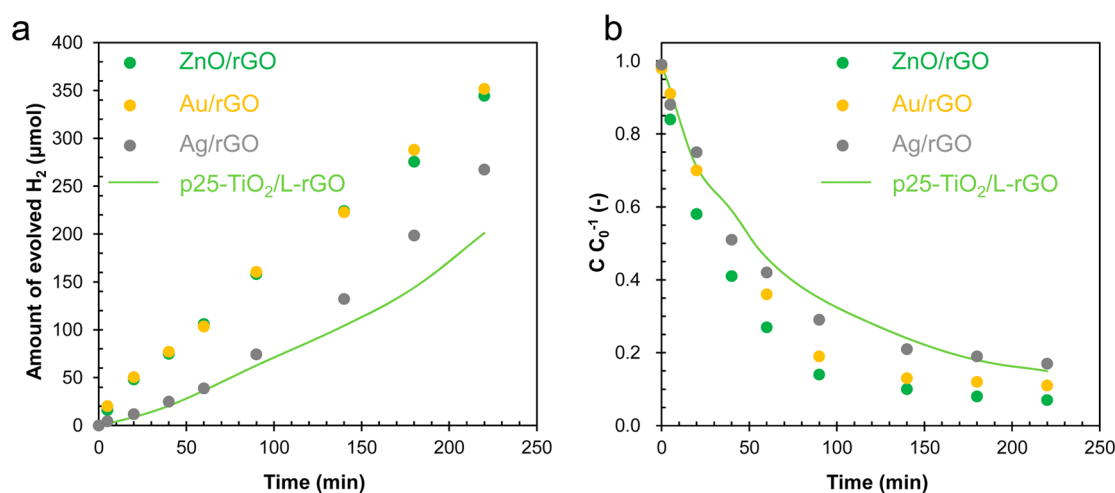


Figure 7. Photocatalytic performances of other hybrid nanoflakes in hydrogen production and dye degradation. (a) Time profiles of hydrogen production with ZnO/rGO ($1.565 \pm 0.133 \mu\text{mol min}^{-1}$), Au/rGO ($1.598 \pm 0.159 \mu\text{mol min}^{-1}$), and Ag/rGO ($1.215 \pm 0.109 \mu\text{mol min}^{-1}$) nanoflakes. (b) Photocatalytic degradations of RhB by ZnO/rGO ($6.58 \times 10^{-3} \pm 0.25 \times 10^{-3} \text{ min}^{-1}$), Au/rGO ($6.02 \times 10^{-3} \pm 0.38 \times 10^{-3} \text{ min}^{-1}$), and Ag/rGO ($5.61 \times 10^{-3} \pm 0.22 \times 10^{-3} \text{ min}^{-1}$) nanoflakes.

Table 2. Summary of the Size Distributions of Spark-Produced ZnO, Au, and Ag, and Their Hybridized Nanostructures with rGO Nanoflakes in the Gas-Phase

case	GMD (nm)	GSD	TNC ($\times 10^6$ particles cm^{-3})
ZnO	43.4	1.57	9.74
ZnO/rGO	42.1	1.56	6.90
Au	24.0	1.50	8.32
Au/rGO	25.3	1.57	2.33
Ag	8.8	1.32	1.96
Ag/rGO	30.5	1.58	1.10

present study is clearly different from the previous ones in that the rGO and TiO_2 were organized into a nanoscale platform. In the present method, the ultrafine TiO_2 particles were

homogeneously attached to the rGO nanoflakes, and this led to good connections between TiO_2 and rGO, which favored a better photocatalytic property and which more effectively oxidized the dye molecules. To verify the morphological revolution, nitrogen adsorption measurements (via a Micromeritics ASAP 2010 apparatus) with the Brunauer, Emmett, and Teller (BET) method was used to determine the surface area of the hybrid materials and to check the possibility of interconnected pores in the materials (Figure 4d). The overall shapes of the samples indicate their meso- and macro-porous characteristics. Since the structure of TiO_2 incorporated with rGO in the gas-phase could result in a remarkable enhancement of the porosity, the BET specific area of TiO_2/rGO was enhanced from 156 to $289 \text{ m}^2 \text{ g}^{-1}$ upon the gas-phase self-assembly between the ultrafine TiO_2 particles and the rGO

nanoflakes. The number N of primary particles constituting the agglomerate after passing through the orifice was smaller than it would be for spark produced TiO_2 particles (see Figure 2a and eq 2, where k_g is the fractal prefactor, D_{p0} is the size of a primary TiO_2 particle, and d_f is the fractal dimension).

$$N = k_g \left(\frac{D_{pr}}{D_{p0}} \right)^{d_f} \quad (2)$$

Therefore, the actual number N_a of TiO_2 particles to be incorporated with rGO is increased by decreasing N (see eq 3, where N_p is the number of primary TiO_2 particles), and subsequently, their total surface area S increased (see eq 4, where m_{TiO_2} is the unit mass of the TiO_2 particles).

$$\frac{N_p}{N} = N_a \quad (3)$$

$$S \approx \frac{N_a \pi D_{pa}^2}{m_{\text{TiO}_2}} \quad (4)$$

As a consequence, TiO_2/rGO could allow an enhancement in the occupation of methanol and RhB molecules on sites between TiO_2 and rGO as a result of the porous structure developed by gas-phase self-assembly.

As a significant expansion of this work, Figures 5–7 show the size distributions, morphologies, and photocatalytic activities of other hybrid nanoflakes from different spark configurations (Zn–Zn under air, Au–Au and Ag–Ag under nitrogen) to verify the generalizability of the gas-phase self-assembly. As shown in Figure 5, even though the other hybrid nanoflakes display different intrinsic size distributions due to different material combinations the size distributions of the metallic nanoparticles converged toward the rGO size distribution (refer to Figure 1), and there was no bimodal distribution character. This implies that the gas-phase self-assembly may induce selective deposition of nanoparticles on the nanoscale rGO matrix. Details of the size distributions are summarized in Table 2. Figure 6 shows that the morphology of ZnO/ and Au/, and Ag/rGO hybrid nanoflakes do not show significant differences among the gas-phase self-assembly cases, although the carrier gas or spark electrode for the synthesis was changed. Details of the crystalline structure of the spark produced ZnO, Au, and Ag particles are described in the previous reports.^{20,26,27} There was only a difference in the morphology of the deposited metallic particles. This proves that the gas-phase self-assembly of the rGO nanoflakes with metallic nanoparticles is generalizable although the material is changed. We further performed photocatalytic activities in hydrogen production and dye degradation and compared the results to p25- $\text{TiO}_2/\text{L-rGO}$. Even though there were differences in the photocatalytic activity, all the gas-phase synthesized samples had a better performance than those from p25- $\text{TiO}_2/\text{L-rGO}$. The performance differences between the samples may have originated from their intrinsic structures, but it is very difficult to synthesize hybrid nanoflakes having the same morphology, size, and crystalline structure for different material combinations. Therefore, we cannot simply discuss the performance difference in photocatalysis between the samples; nevertheless, one can conclude that the gas-phase self-assembly of rGO with metallic particles in a nanoscale matrix possibly has the most synergetic effect accounting for the enhanced photocatalytic activities.

CONCLUSIONS

We developed for the first time a continuous gas-phase synthesis of TiO_2/rGO nanoflakes as a green and generalizable process; the nanoflakes have a self-assembled hybrid nanostructure, and we also tested their photocatalytic activities. All previous TiO_2/rGO hybrid materials employed micrometer-sized sheets of graphene on which TiO_2 nanoparticles were loaded. Compared with p25- $\text{TiO}_2/\text{L-rGO}$, there is more contact area between the rGO nanoflakes and the ultrafine TiO_2 particles. The unique hybrid structure enabled better contact between the rGO and TiO_2 and facilitated efficient electron transfer for better photocatalytic activities in the energy and environmental fields. The proposed method opens up a new way to obtain photoactive graphene-based hybrid nanomaterials for a broad range of practical applications.

ASSOCIATED CONTENT

Supporting Information

Production of GO and other characterizations. This material is available free of charge via the Internet at <http://pubs.acs.org/>.

AUTHOR INFORMATION

Corresponding Author

*Tel.: +82 41 540 5819. Fax: +82 41 540 5818. E-mail: ywkim@hoseo.edu.

Notes

The authors declare no competing financial interest.

ACKNOWLEDGMENTS

This research was supported by the Academic Research Fund of Hoseo University in 2012 (2012-0301).

REFERENCES

- (1) Wu, T.; Liu, S.; Luo, Y.; Lu, W.; Wang, L.; Sun, X. *Nanoscale* **2011**, 3, 2142–2144.
- (2) Pan, Y.; Bao, H.; Li, L. *ACS Appl. Mater. Interfaces* **2011**, 3, 4819–4830.
- (3) Ding, Y. H.; Zhang, P.; Zhuo, Q.; Ren, H. M.; Yang, Z. M.; Jiang, Y. *Nanotechnology* **2011**, 22, 215601.
- (4) Huang, X.; Zhou, X.; Zhou, L.; Qian, K.; Wang, Y.; Liu, Z.; Yu, C. *ChemPhysChem* **2011**, 12, 278–281.
- (5) Zhou, X.; Huang, X.; Qi, X.; Wu, S.; Xue, C.; Boey, F. Y. C.; Yan, Q.; Chen, P.; Zhang, H. *J. Phys. Chem. C* **2009**, 113, 10842–10846.
- (6) Yao, J.; Shen, X.; Wang, B.; Liu, H.; Wang, G. *Electrochem. Commun.* **2009**, 11, 1849–1852.
- (7) Shah, Md. S. A. S.; Park, A. R.; Zhang, K.; Park, J. H.; Yoo, P. J. *ACS Appl. Mater. Interfaces* **2012**, 4, 3893–3901.
- (8) Fan, W.; Lai, Q.; Zhang, Q.; Wang, Y. *J. Phys. Chem. C* **2011**, 115, 10694–10701.
- (9) Yang, K.; Feng, L.; Shi, X.; Liu, Z. *Chem. Soc. Rev.* **2013**, 42, 530–547.
- (10) Zhang, H.; Lv, X.; Li, Y.; Wang, Y.; Li, J. *ACS Nano* **2010**, 4, 380–386.
- (11) Kim, H.-i.; Moon, G.-h.; Monllor-Satoca, D.; Park, Y.; Choi, W. *J. Phys. Chem. C* **2012**, 116, 1535–1543.
- (12) Shen, J.; Shi, M.; Yang, B.; Ma, H.; Li, N.; Ye, M. *J. Mater. Chem.* **2011**, 21, 7795–7801.
- (13) Mayavan, S.; Sim, J.-B.; Choi, S.-M. *J. Mater. Chem. C* **2012**, 22, 6953–6958.
- (14) Li, Y.; Lv, X.; Lu, J.; Li, J. *J. Phys. Chem. C* **2010**, 114, 21770–21774.
- (15) Sun, X.; Liu, Z.; Welsher, K.; Robinson, J. T.; Goodwin, A.; Zaric, S.; Dai, H. *Nano Res.* **2008**, 1, 203–212.
- (16) Byeon, J. H.; Park, J. H.; Hwang, J. *J. Aerosol Sci.* **2008**, 39, 888–896.

- (17) Byeon, J. H.; Roberts, J. T. *ACS Appl. Mater. Interfaces* **2012**, *4*, 2693–2698.
- (18) Byeon, J. H.; Kim, J.-W. *Appl. Phys. Lett.* **2012**, *101*, 023117.
- (19) Byeon, J. H.; Roberts, J. T. *Chem. Mater.* **2012**, *24*, 3544–3549.
- (20) Byeon, J. H.; Kim, J.-W. *Langmuir* **2010**, *26*, 11928–11933.
- (21) Guardia, L.; Villar-Rodil, S.; Paredes, J. I.; Rozada, R.; Martínez-Alonso, A.; Tascón, J. M. D. *Carbon* **2012**, *50*, 1014–1024.
- (22) Min, Y.; Zhang, K.; Chen, L.; Chen, Y.; Zhang, Y. *Synth. Met.* **2012**, *162*, 827–833.
- (23) Liu, J.; Bai, H.; Wang, Y.; Liu, Z.; Zhang, X.; Sun, D. D. *Adv. Funct. Mater.* **2010**, *20*, 4175–4181.
- (24) Chen, L.; Chen, F.; Shi, Y.; Zhang, J. J. *Phys. Chem. C* **2012**, *116*, 8579–8586.
- (25) Haro, M.; Velasco, L. F.; Ania, C. O. *Catal. Sci. Technol.* **2012**, *2*, 2264–2272.
- (26) Byeon, J. H.; Kim, J.-W. *J. Colloid Interface Sci.* **2013**, *393*, 397–401.
- (27) Byeon, J. H.; Kim, J.-W. *Thin Solid Films* **2010**, *519*, 700–705.